# Photoelectric Activity of a $Bi_2O_3/Bi_2WO_{6-x}F_{2x}$ Heterojunction Prepared by a Simple One-Step Microwave Hydrothermal Method

Jing Huang, Guoqiang Tan,* Huijun Ren, Wei Yang, Chi Xu, Chengcheng Zhao, and Ao Xia

Key Laboratory of Auxiliary Chemistry & Technology for Chemical Industry, Ministry of Education, Shaanxi University of Science & Technology, Xi'an 710021, China

ABSTRACT: NH_4F/Bi_2WO_6 powders were prepared by a simple one-step microwave hydrothermal method at different reaction temperatures, using $Bi(NO_3)_3 \cdot 5H_2O$ and $Na_2WO_4 \cdot 2H_2O$ as raw materials and NH_4F as an additive agent. Their photoelectric activities were also investigated via the degradation of Rhodamine B (RhB). The results indicate that when the reaction temperature increases to 220 and 240 °C, the orthorhombic Bi_2WO_6 phase with space group $Pca21$ and cubic Bi_2O_3 phase with space group $Pn\bar{3}m$ appear. Raman spectroscopy, SEM, TEM, and XPS results also confirm the existence of a $Bi_2O_3/Bi_2WO_{6-x}F_{2x}$ heterojunction at higher temperature. Greater than 95% photodegradation of RhB under the exposure of simulated sunlight is achieved within 90 min with the $Bi_2O_3/Bi_2WO_{6-x}F_{2x}$ heterojunction prepared at 220 °C, which displays remarkably promoted photocatalytic activities. The electrochemical impedance spectra and photocurrent results also prove that efficient charge separation and better electron transport properties are achieved by the $Bi_2O_3/Bi_2WO_{6-x}F_{2x}$ heterojunction film prepared at 220 °C. In addition, the mechanism of the crystal growth and formation of the $p-n$ junction between p-type Bi_2O_3 and n-type Bi_2WO_6 were also discussed.

KEYWORDS: NH_4F/Bi_2WO_6, $Bi_2O_3/Bi_2WO_{6-x}F_{2x}$, hererojunction, microwave-hydrothermal method, reaction temperature, photoelectric activities
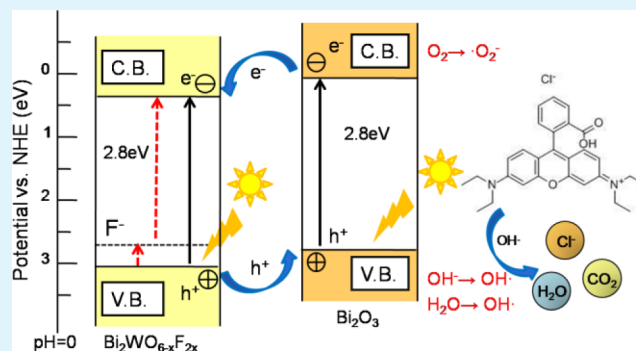
1. INTRODUCTION

Heterogeneous photocatalysis is an advanced oxidation technology that can be applied to solve environmental and energy problems.[1−3] Many efforts have been made to develop efficient photocatalysts, which could maximally utilize the clean, safe, and abundant solar energy. Among them, Bi_2WO_6 is one of the simplest Aurivillius oxides, which possesses layered structure with the perovskite-like slab of WO_6 and exhibits excellent photocatalytic activities for the decomposition of a great variety of organic pollutants in environmental purification applications.[4−9]

However, the photocatalytic application is restricted, because of its rapid recombination with photogenerated charge carriers. Therefore, it is necessary to take some measures to improve the migration efficiency of photoinduced electrons and suppress the recombination of electrons and holes effectively. Some of the most feasible modifications are doping (cationic or anionic) and metal deposition. For example, the modifications of Bi_2WO_6 with Ag nanoparticles,[10] C_{60},[11] and Co_3O_4[12] have been reported to inhibit the recombination of photogenerated holes and electrons effectively, and, thus, the photocatalytic activity is greatly improved. Clearly, both the photocatalyst composition and its structure are important.

Recently, the composite semiconductor photocatalysts have received great attention, because of their enhanced photo-catalytic activities.[13−16] In composite semiconductors, some advantages can be achieved: an improvement of charge separation, an increase in the lifetime of the charge carrier, and an enhancement of the interfacial charge transfer efficiency to adsorbed substrate.[17] Moreover, to improve its quantum efficiency, many researchers have coupled Bi_2WO_6 with other semiconductors, such as TiO_2,[18,19] Ag_3PO_4,[20] $BiOCl$,[21] and ZnO.[22]

Besides these, some research groups reported that Bi_2O_3/Bi_2WO_6 composite had higher degradation performance than that of pure Bi_2WO_6.[23−25] By far, the templated method is the most effective method in the preparation of the Bi_2O_3/Bi_2WO_6 composite.[26] However, it is well-known that many reaction conditions, such as the concentration of precursor, reaction temperature, and time, have important effects on the crystalline phase and morphology of the powders.[27,28]

Herein, we report the synthesis of a $Bi_2O_3/Bi_2WO_{6-x}F_{2x}$ composite (composed of nanosheets) through a simple one-step microwave hydrothermal route without any template and any other treatment, which can be called an in situ process and is beneficial for the formation of heterojunction interfaces.
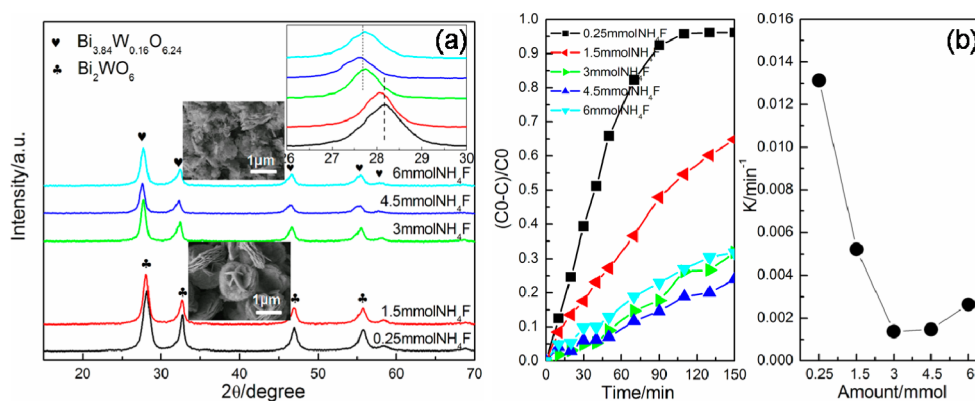
Figure 1. (a) XRD patterns of NF/BWO samples synthesized at 180 °C for 60 min with different content of NH$_4$F. (b) Photocatalytic degradation rate of RhB and reaction rate constant of NF/BWO samples with different NH$_4$F contents.

Meanwhile, we study the influence of different temperatures on morphology, structure and photoelectric activities of the products. It focuses on the impact on the structure and morphology of Bi$_2$WO$_6$ formed by microwave reaction (temperature-assisted), using an NH$_4$F additive agent.

2. EXPERIMENTAL SECTION

2.1. Preparation. *2.1.1. Powder Samples.* All of the reagents were of analytical grade and were used without any further purification. The typical preparation of NH$_4$F/Bi$_2$WO$_6$ (NF/BWO) samples was as follows: First, 6 mmol of Bi(NO$_3$)$_3$·5H$_2$O and 3 mmol of Na$_2$WO$_4$· 2H$_2$O were added simultaneously into 60 mL of distilled water with strong magnetic stirring at room temperature for 30 min. Second, x mmol of NH$_4$F were added to the solution (x = 0.25, 1.5, 3, 4.5, 6). The resulting solution was then stirring sequentially until all reagents were dispersed homogeneously. Subsequently, the mixture was transferred into a 100-mL Teflon-lined autoclave. The autoclave was sealed and maintained at different temperatures (160, 180, 220, 240 °C) for 60 min, then cooled to room temperature naturally. The precipitates were collected and washed for several times with distilled water and absolute ethyl alcohol, respectively. Finally, the products were obtained and dried at 70 °C for 12 h.

2.1.2. Film Electrode. A total of 0.1 g of synthesized powder sample was added into a mixed solution with 1 mL of anhydrous ethanol and 0.1 mL of acetyl acetone. After a period of time, it became a stable suspension with ultrasonic dispersion. The powder then was spread out onto a 1.5 cm × 2 cm FTO glass substrate with spin-coating method for 5 times. After liquid volatilization, this membrane electrode was calcinated at 150 °C for 3 h.

2.2. Characterization. The crystalline structures of the samples were characterized by a powder X-ray diffraction (XRD) using a Rigaku Model D/max-2200PC system for Cu Kα radiation (λ = 0.15406 nm) at 40 kV and 40 mA. The morphologies and microstructures characterizations were performed on the field-emission scanning electron microscopy (FE-SEM) (JEOL, Model JSM-6700F) and transmission electron microscopy (TEM) (FEI TECNAI, Model G^{2}F20 S-TWIN, USA) systems. The specific surface area was measured by a specific surface area analyzer (BJ, Model 3H-2000BET-A, China). The adsorbate was N$_2$, while the carrier gas was helium. The surface analysis was studied by X-ray photoelectron spectroscopy (XPS) (Model XSAM800, Shimadzu−Kratos Ltd., Japan). The binding energy data was calibrated with the C 1s signal at 284.6 eV. Raman scattering spectra were performed with an Ar$^+$-ion laser excitation at 532 nm (Horiba, Model JY HR800).

2.3. Electrochemical Analyses. Electrochemical impedance spectroscopy (EIS) and chronoamperometry experiments were conducted using an electrochemical workstation (Model CHI660E, CH Instruments, China). Such experiments were performed in the frequency range between 0.05 Hz and 100 kHz with a voltage amplitude of 5 mV at a initial voltage of 1.2 V. Electrochemical

analyses were performed using a standard three-electrode cell with platinum used as a counter electrode and a saturated Ag/AgCl electrode used as a reference electrode. The NF/BWO nanostructure coated FTO plates were suspended in 0.1 mol/L Na$_2$SO$_4$ aqueous electrolyte as a working electrode. All the experiments were conducted at room temperature. The impedance spectra were interpreted by a nonlinear least-squares fitting procedure using commercial software (ZsimpWin). A Xe lamp (350 W) was used as a light source for simulated sunlight irradiation in photoelectrochemical analyses.

2.4. Photocatalytic Activity. Photocatalytic activities of the samples were evaluated by the degradation of Rhodamine B (RhB) under visible light irradiation of a 350 W Xe lamp. The degradation reactions were conducted in an XPA-7 photochemical reactor (Xujiang Machine Factory, Nanjing, China). In each experiment, 0.05 g of photocatalyst was added into 50 mL RhB solution (1 × 10^{-5} mol/L) and the solution was stirred in darkness for 1 h before illumination to ensure the equilibrium of an adsorption−desorption equilibrium between the photocatalyst and RhB. At a certain period of time, 6 mL of suspension was taken out and centrifuged to remove the photocatalyst particles. The concentrations of the RhB solutions then were analyzed using an ultraviolet−visible light (UV-vis) spectrophotometer (Model SP-756P, Shanghai Optical Spectrometer Company).

3. RESULTS AND DISCUSSION

3.1. Analysis of NF/BWO with Different Content. Figure 1a shows XRD patterns of NF/BWO samples synthesized at 180 °C for 60 min with different NH$_4$F contents. Figure 1a shows that the NH$_4$F content influenced the phase of the samples. When the NH$_4$F content was 0.25 mmol, the product was orthorhombic Bi$_2$WO$_6$ structure (JCPDS No. 39-0256), whereas with the increases in NH$_4$F, the crystallinity of orthorhombic Bi$_2$WO$_6$ was destroyed, illustrating that the impurity ions destroyed the normal growth and the development of Bi$_2$WO$_6$ grains. The phase of the product changed with the addition of 3 mmol of NH$_4$F, generating nonstoichiometric Bi$_{3.84}$W$_{0.16}$O$_{6.24}$ (JCPDS No. 43-0447). In addition, the morphologies of the products with 1.5 mmol NH$_4$F and 6 mmol NH$_4$F were obviously different, as can be seen from the inset, which showed a laminar 1-μm-thick layer structure of Bi$_2$WO$_6$ and small irregularly shaped Bi$_{3.84}$W$_{0.16}$O$_{6.24}$ particles. The photocatalytic results demonstated that the photocatalytic activitiy of the sample with the addition of 0.25 mmol of NH$_4$F was optimum (Figure 1b). The degradation rate of RhB was more than 90% after illumination for 90 min. The reaction rate constant (K) also proved this point (0.013 min^{-1}), which is apparently higher than that of other samples. This showed that different NH$_4$F contents
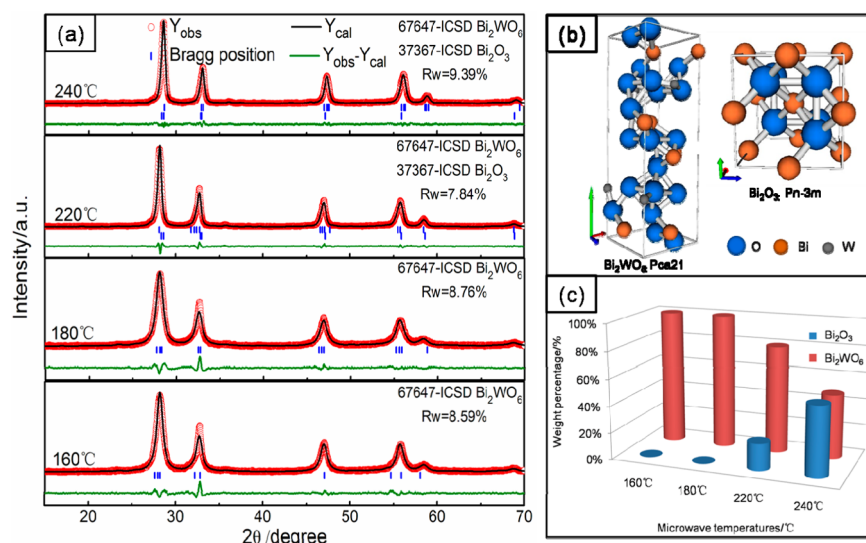
Figure 2. (a) Rietveld refinement, (b) crystal structure, and (c) component result of NF/BWO sample (0.25 mmol NH$_4$F) at different reaction temperatures.

Table 1. Cell Parameters by Rietveld Refinement of NF/BWO Sample (0.25 mmol NH$_4$F) at Different Reaction Temperatures

sample	R_w (%)	symmetry	space group	Lattice Parameters		
				a (Å)	b (Å)	c (Å)
160 °C	8.59	orthorhombic Bi$_2$WO$_6$ (100%)	$Pca21$	5.4555	16.3584	5.4575
180 °C	8.76	orthorhombic Bi$_2$WO$_6$ (100%)	$Pca21$	5.4555	16.3641	5.4576
220 °C	7.84	orthorhombic Bi$_2$WO$_6$ (79.95%)	$Pca21$	5.4950	16.3580	5.4441
		cubic Bi$_2$O$_3$ (20.05%)	$Pn\bar{3}m$		5.4433	
240 °C	9.39	orthorhombic Bi$_2$WO$_6$ (48%)	$Pca21$	5.4622	16.4557	5.4950
		cubic Bi$_2$O$_3$ (52%)	$Pn\bar{3}m$		5.4603	

played an important role in the photocatalytic activities. Therefore, the sample with adding 0.25 mmol NH$_4$F was selected as an object to study the influence of different reaction temperature on the crystal structure, the morphology, and the photoelectric activities.

3.2. Analysis of NF/BWO at Different Reaction Temperature. 3.2.1. Structural Analysis. In order to characterize the obtained crystalline material more precisely, the full-profile Rietveld refinement was performed using MAUD and FindIt program.[29,30] The observed, calculated, and the difference refined XRD patterns of NF/BWO powders are shown in Figure 2a. Bi$_2$WO$_6$ adopts orthorhombic $Pca21$ structure with the following lattice parameters: a = 5.4373 Å, b = 16.4302 Å, and c = 5.4584 Å. These reported structural parameters of Bi$_2$WO$_6$,[31] as well as the atomic positions in cubic Bi$_2$O$_3$, were used as starting models for the two-phase full-profile Rietveld refinement.[32] It could be seen that at 160 and 180 °C, sharp and well-defined peaks were observed, in accordance with the Bi$_2$WO$_6$ phase with space group $Pca21$ for orthorhombic russellite structure (ICSD Card No. 67647). However, when the reaction temperature increased to 220 and 240 °C, detailed examination of powder X-ray diffraction (XRD) pattern showed that the diffraction peak had an obvious shift and it was best-fitted to the coexistance of the Bi$_2$WO$_6$ phase and a cubic $Pn\bar{3}m$ Bi$_2$O$_3$ phase (ICSD Card No. 37367), which proved that impurities entered into the crystal lattice, changing the crystal growth environment and generating a new phase at higher temperatures.

Bi$_2$WO$_6$ is the n = 1 member of the family (Bi$_2$O$_2$)-(W$^{6+}_n$O$_{3n+1}$) of cation-deficient bismuth-layered compounds.[33]

In the case of Bi$_2$WO$_6$, the structure consists of alternating layers of corner-shared WO$_6$ octahedra and Bi$_2$O$_2^{2+}$ (Bi$_2$O$_3$) slabs lying perpendicular to the long [010] axis (Figure 2b, left). The Bi$_2$O$_3$ sheets are built up by edge-sharing BiO$_4$ square pyramids where the oxygen atoms form basal planes and the Bi atoms occupy the apex above and below the oxygen basal planes, as shown in Figure 2b (right). Because of similar structure, the structural transformation would occur under the condition of high temperature, high pressure, or NH$_4$F doping.

We could also see, from Figure 2c, that, as the reaction temperature increased, the content of Bi$_2$O$_3$ increased gradually. When the temperature was 240 °C, the contents of Bi$_2$WO$_6$ and Bi$_2$O$_3$ were basically the same. As shown in Table 1, it could be clearly observed that, as the temperature increased, the cell parameters of Bi$_2$WO$_6$ became larger, indicating that NH$_4$F impurity entered into the crystal structure at higher temperature and changed the lattice growth.

Raman spectroscopy is a powerful and nondestructive experimental technique for probing vibrational and structural properties of materials. Figure 3 showed the Raman scattering spectrum of NF/BWO samples at different temperatures, obtained in ambient atmosphere with an excitation wavelength of 532 nm. Both the observations demonstrated that the reaction temperature had a significant effect on the Raman property of NF/BWO, indicating a strong interaction between Bi$_2$WO$_6$ and NH$_4$F. It could be seen that the spectra of NF/BWO samples at 220 and 240 °C were quite different from the samples at 160 and 180 °C, which indicated some crystal transition in the system.
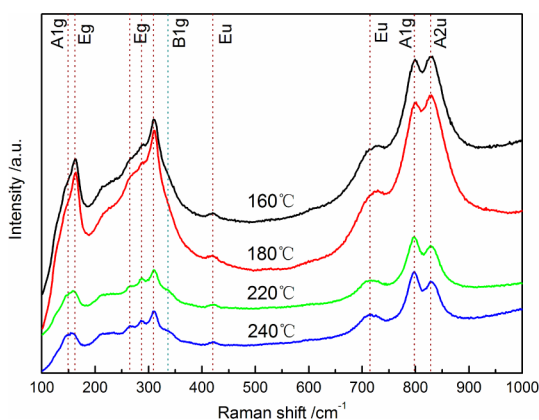
Figure 3. Raman scattering spectrum of NF/BWO sample (0.25 mmol NH_4F) at different reaction temperatures.

The bands in the 180−600 cm^{-1} originated from the bending modes of the WO_6 octahedrons coupled with the bending modes of the bismuth−oxygen polyhedrons. The bending of WO_6 octahedrons consisted of the 260 (Eu), 282 (Eg), 306 (Eg), and 415 (Eu) cm^{-1}. The bending of Bi−O polyhedrons was observed at 332 (B1g) cm^{-1}. In more detail, the bands observed at 145 and 151 cm^{-1} may be assigned to the lattice modes of the Bi ions.[34−36] The peaks in the range 600−1000 cm^{-1} can be assigned to the stretching modes of the W−O bands.[37] The weak Raman peaks in the 700−740 cm^{-1} range were due to asymmetric (Eu) stretching modes of the WO_6 octahedrons, which mainly involved the vibrations of equatorial O atoms. The bands of 795 and 828 cm^{-1} can be assigned to the symmetric and antisymmetric stretching Ag modes of terminal O−W−O groups, respectively, which involved the motions of apical oxygen atoms. Pure Bi_2O_3 shows several strong Raman bands at 212, 282, 315, and 412 cm^{-1}.[38]

However, these could not be detected clearly at 220 and 240 °C. It may be that the characteristic peaks of Bi_2O_3 were too weak to check out or be hidden behind the peaks of Bi_2WO_6. This phenomenon was possibly due to molecular polarization and the degree of crystallinity.

3.2.2. Morphological Analysis. The heterostructure of the NF/BWO sample at different temperatures is shown in Figure 4. When the reaction temperature was 160 °C, the NF/BWO sample was composed of irregular nanosheets ∼10 nm thick, as shown in Figure 4a. The high-resolution transmission electron microscopy (HRTEM) image and the selected-area electron diffraction (SAED) of a single nanosheet (Figure 4b) exhibited a single crystalline structure. The lattice spacing of 0.273 nm corresponded to the *d*-spacing between adjacent (002) planes of Bi_2WO_6, indicating that crystalline Bi_2WO_6 was generated at low temperature. As the temperature increased to 180 °C, the nanosheets gradually grew and assembled into a 2-μm hollow flower-like structure (see Figure 4b). The lattice spacing of 0.274 nm corresponded to the interplanar distance between adjacent (060) crystallographic planes of Bi_2WO_6, shown in Figure 4d. However, the morphology and structure of the sample were changed significantly at higher temperature (220 °C), displaying uniform and regular square nanoflakes in Figures 4e and 4f; in addition, a few small particles adhered on the surface of the nanoflakes, as shown in Figure 4g. The HRTEM image of the composite showed two types of intimately contacted lattice fringes, confirming a Bi_2O_3/ Bi_2WO_6 nanocrystal heterojunction formed in the composite (Figure 4h). The lattice spacing of 0.273 and 0.274 nm corresponded to the interplanar distance between (002) and (060) crystallographic planes of Bi_2WO_6, while the fringe of *d* = 0.314 nm matched that of the (111) plane of Bi_2O_3, corresponded with the above Rietveld refinement results. In addition, the morphology and the structure of the sample prepared at 240 °C were similar to that at 220 °C (Figures 4i−
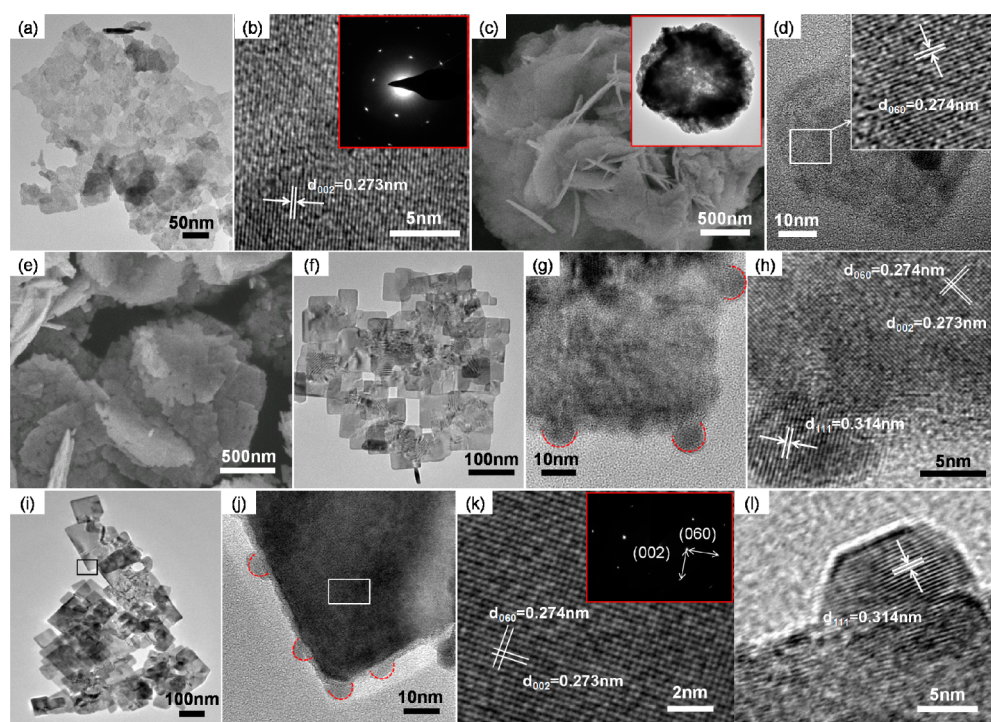

Figure 4. SEM, TEM, HRTEM, and SAED images of NF/BWO powder at (a,b) 160 °C, (c,d) 180 °C, (e−h) 220 °C, and (i−l) 240 °C.
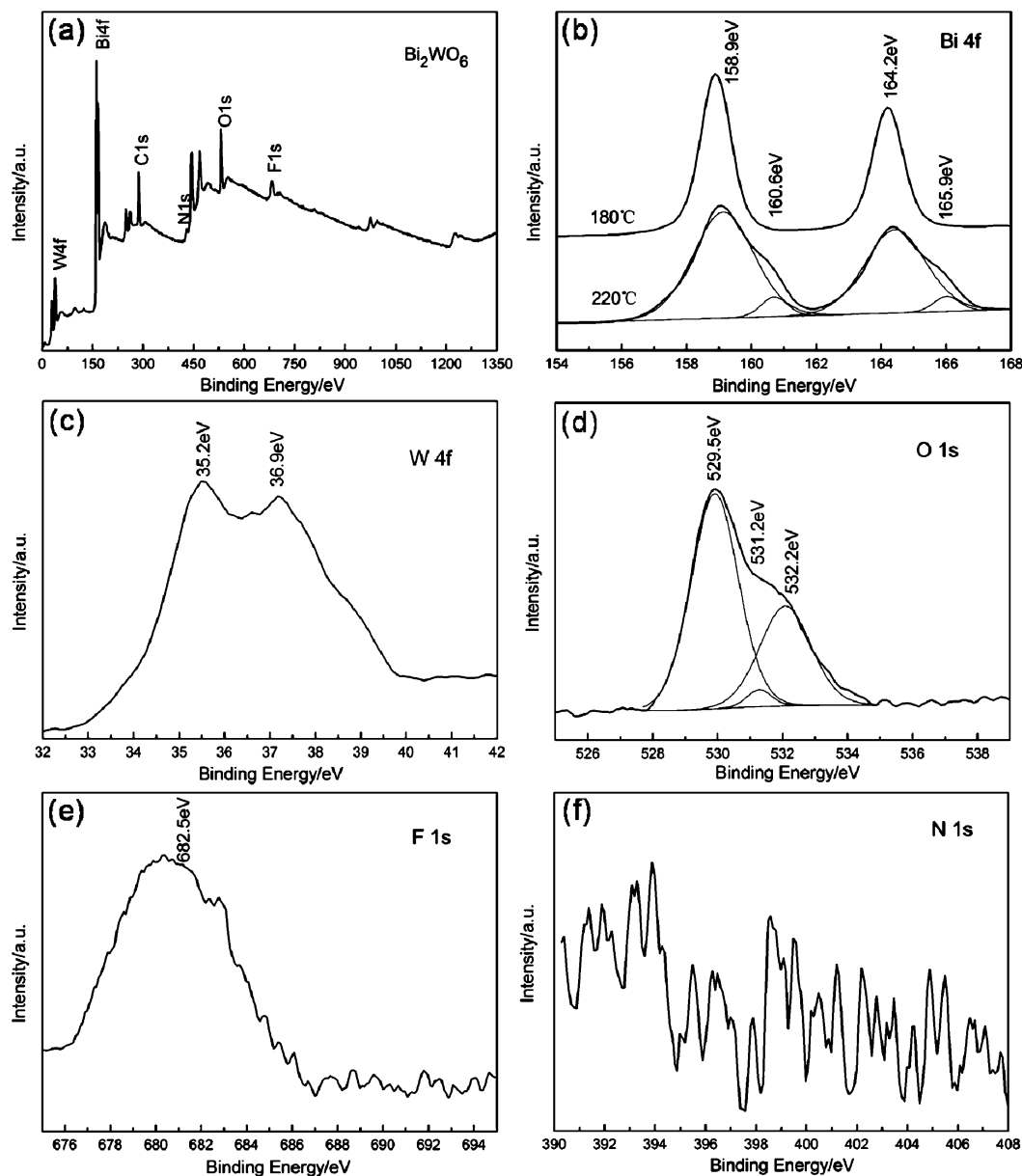
Figure 5. XPS spectra of NF/BWO sample (0.25 mmol NH₄F) prepared at 220 °C: (a) full spectrum, (b) Bi 4f (compared with 180 °C), (c) W 4f, (d) O 1s, (e) F 1s, and (f) N 1s.
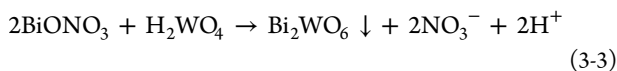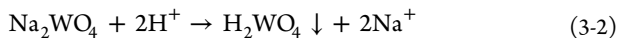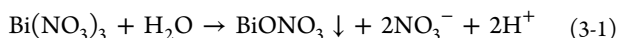
l). The above results illustrated that the sample grew to two-dimensional nanosheets at low temperature, and then assembled to a hollow center structure. As the temperature increased further, it was destroyed by impurities and became square nanoflakes, accompanying the generation of Bi_2O_3. However, the increase of temperatures reduced the specific surface area of the samples. The specific surface area of the sample prepared from 160 °C to 240 °C was 30.04, 32.79, 18.84, and 14.80 m^2/g, respectively. Large specific surface area tends to expose more coordination unsaturated sites on the surface of the sample and more reactant can be absorbed onto the surface, which is favorable for the redox reaction. Previous studies proved that the formation of this heterostructure was not only affected by the temperature, but also on the basis of the impurities.[39] Its growth mechanism would be particularly discussed later.

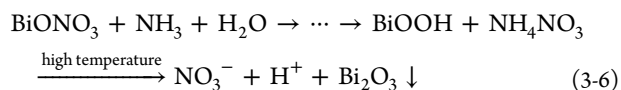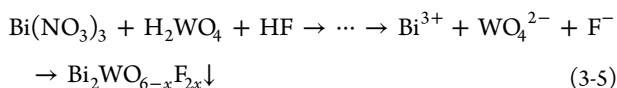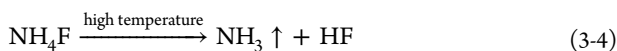*3.2.3. Mechanism of Crystal Growth.* X-ray photoelectron spectroscopy (XPS) surface measurements were taken on NF/

BWO with 0.25 mmol NH₄F at 220 °C to determine the surface compositions and chemical states of the samples, shown in Figure 5. The binding energies obtained in the XPS analysis were corrected for specimen charging by reference to a C 1s value of 284.6 eV. Figures 5b–d are high-resolution XPS spectra of three primary elements: Bi 4f, W 4f, and O 1s, respectively. The high-resolution XPS spectra of the Bi 4f$_{7/2}$ region (220 °C) could be fitted into two peaks at ~158.9 and 160.6 eV, which suggested that there were two types of Bi ions in the as-prepared NF/BWO composite (Figure 5b). Considering that the binding energy of the Bi ion in pure Bi_2WO_6 existed in the range of 158–159 eV and that for Bi_2O_3 existed in the range of 159–160 eV,[40,41] the peak at 158.9 eV could be ascribed to Bi^{3+} in Bi_2WO_6, while the other one at 160.6 eV originated from Bi^{3+} in Bi_2O_3. The same phenomenon happened in the XPS spectra of Bi 4f$_{5/2}$ region resulting in the peaks at 164.2 and 165.9 eV. Compared with the high-temperature results, XPS spectra of the Bi region prepared at

21045

dx.doi.org/10.1021/am505817h | *ACS Appl. Mater. Interfaces* 2014, 6, 21041−21050

180 °C indicated that only peaks at 158.6 and 164 eV could be observed, which proved that only Bi_2WO_6 existed at lower temperatures. In Figure 5c, the XPS spectrum in the W 4f region showed a binding energy at 35.2 and 36.9 eV, which was 0.5 eV different from W^{6+} reported previously.[12] It was due to the peak of F 1s region (Figure 5e), which showed that F ions entered into the lattice of Bi_2WO_6 and destroyed the characteristic peaks of the W $4f_{5/2}$ and W $4f_{7/2}$ spin−orbit. Because of the smaller radius than O, it would form a stronger binding energy (F−W−O) when F replaced partial O ions (generation of $Bi_2WO_{6-x}F_{2x}$), resulting in the peak shift of the W 4f region. The XPS spectrum in the O 1s region is shown in Figure 5d. It was found that the O 1s region of NF/BWO could be fitted into three peaks, which can be attributed to Bi−O (532.2 eV) in Bi_2O_3, W−O (531.2 eV), and Bi−O (529.5 eV) in Bi_2WO_6, respectively.[42] Also the binding energy of N 1s was weak (Figure 5f), which explained the difficulty for N to enter into the crystal lattice. The results revealed the coexistence of Bi_2O_3 and Bi_2WO_6 at higher temperatures, which was in good agreement with the above analysis.

Based on the above research and our previous report,[39] the generation of a $Bi_2O_3/Bi_2WO_{6-x}F_{2x}$ heterojunction occurs based on the conditions (e.g., the presence/absence of the NH_4F impurity and the reaction temperature). The growth process of $Bi_2O_3/Bi_2WO_{6-x}F_{2x}$ grain was as follows: $Bi(NO_3)_3$ and Na_2WO_4 were dissolved in aqueous solution at room temperature, occurring as a reaction type of hydrolysis process (see reactions 3-1 and 3-2. Under the condition of low temperature, $BiONO_3$ and H_2WO_4 reacted to generate Bi_2WO_6 (see reaction 3-3. In the initial stage of microwave hydrothermal reaction, the connection between precursor particles ($BiONO_3$ and H_2WO_4) was destroyed, thus causing $BiONO_3$ and H_2WO_4 particles to dissolve in the system, existing in the form of BiO^+ and WO_4^{2-} ions in solution. When the concentration of BiO^+ and WO_4^{2-} ions was higher than the saturation for grain nucleation, BiO^+ and WO_4^{2-} ions would form a Bi_2WO_6 crystal nucleus and the grain growth would eventually occur.

$$Bi(NO_3)_3 + H_2O \rightarrow BiONO_3 \downarrow + 2NO_3^- + 2H^+ \quad (3\text{-}1)$$

$$Na_2WO_4 + 2H^+ \rightarrow H_2WO_4 \downarrow + 2Na^+ \quad (3\text{-}2)$$

$$2BiONO_3 + H_2WO_4 \rightarrow Bi_2WO_6 \downarrow + 2NO_3^- + 2H^+ \quad (3\text{-}3)$$

However, when the NH_4F impurity was added into the reaction system, it would form NH_3 and HF at high temperature (see reaction 3-4), both of which increase the pressure in the microwave autoclave. The pressure, high temperature, and strong acidic conditions made it easier for F ions to enter into the crystal lattice of Bi_2WO_6. On the one hand, $Bi_2WO_{6-x}F_{2x}$ was formed (see reaction3-5, which describes dissolution and recrystallization); on the other hand, lattice distortion occurred subsequently, changing the generation of the Bi−O bond and making the Bi_2O_3 crystallite grow, eventually forming a $Bi_2O_3/Bi_2WO_{6-x}F_{2x}$ hererojunction (see reaction 3-6).

$$NH_4F \xrightarrow{\text{high temperature}} NH_3 \uparrow + HF \quad (3\text{-}4)$$

$$Bi(NO_3)_3 + H_2WO_4 + HF \rightarrow \cdots \rightarrow Bi^{3+} + WO_4^{2-} + F^-$$
$$\rightarrow Bi_2WO_{6-x}F_{2x}\downarrow \quad (3\text{-}5)$$

$$BiONO_3 + NH_3 + H_2O \rightarrow \cdots \rightarrow BiOOH + NH_4NO_3$$
$$\xrightarrow{\text{high temperature}} NO_3^- + H^+ + Bi_2O_3 \downarrow \quad (3\text{-}6)$$

3.2.4. Photocatalytic Performance Analysis. The photocatalytic properties of the as-synthesized samples were measured by monitoring the change in optical absorption of the RhB solution at 554 nm during its photocatalytic decomposition process. As shown in Figure 6, the degradation
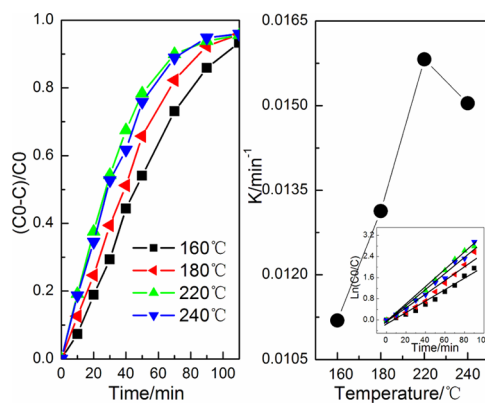

Figure 6. (a) Photocatalytic degradation rate of RhB and (b) reaction rate constant of NF/BWO sample (0.25 mmol NH_4F) at different reaction temperatures.

of all samples exceeded 90% after illumination for ∼110 min. However, the process was different, showing that the reaction rate constants (K) at 220 and 240 °C were much higher than those at 160 and 180 °C. The adsorption efficiency of each sample was also calculated as 13.59%, 6.41%, 8.43%, and 1.83%, respectively, after continuing to keep it in a dark enviroment for 1 h, which was related to its specific surface area; however, it was not the main reason for the photocatalytic activities. It indicated that the photocatalytic properties of the $Bi_2O_3/Bi_2WO_{6-x}F_{2x}$ hererojunctions were remarkably promoted, since the degradation of RhB solution simulated sunlight irradiation.

3.2.5. Electrochemical Studies. The electrochemical impedance spectra (EIS) of the as-prepared NF/BWO films were measured under simulated sunlight irradiation. The EIS Nyquist plots were used to investigate the capacitance and resistance of the electrode materials, which indicated that it could confirm the separation efficiency between the photogenerated electron−hole pairs and the property of carriers.[43,44] The Nyquist plot of NF/BWO films at different temperatures are shown in Figure 7 (denoted by data points). The diameter of the Nyquist circular radius decreased significantly before and after the illumination, showing that the impedance and capacitive reactance were reduced, respectively, along with the separation rate of electron−hole pairs and the charge transportation increased greatly. From Figure 7, we could also see that the EIS Nyquist plot of $Bi_2O_3/Bi_2WO_{6-x}F_{2x}$ prepared at 220 and 240 °C exhibited a smaller circular radius than that of other films, which suggested that the charge-transfer resistance of $Bi_2O_3/Bi_2WO_{6-x}F_{2x}$ film was smaller than that of other films.[45] Therefore, we can infer from the EIS Nyquist plot that efficient charge separation and better electron transport properties were achieved by the heterojunction film prepared at higher temperatures.

In order to obtain more-accurate information, the EIS Nyquist plot was simulated by ZsimpWin analysis software.
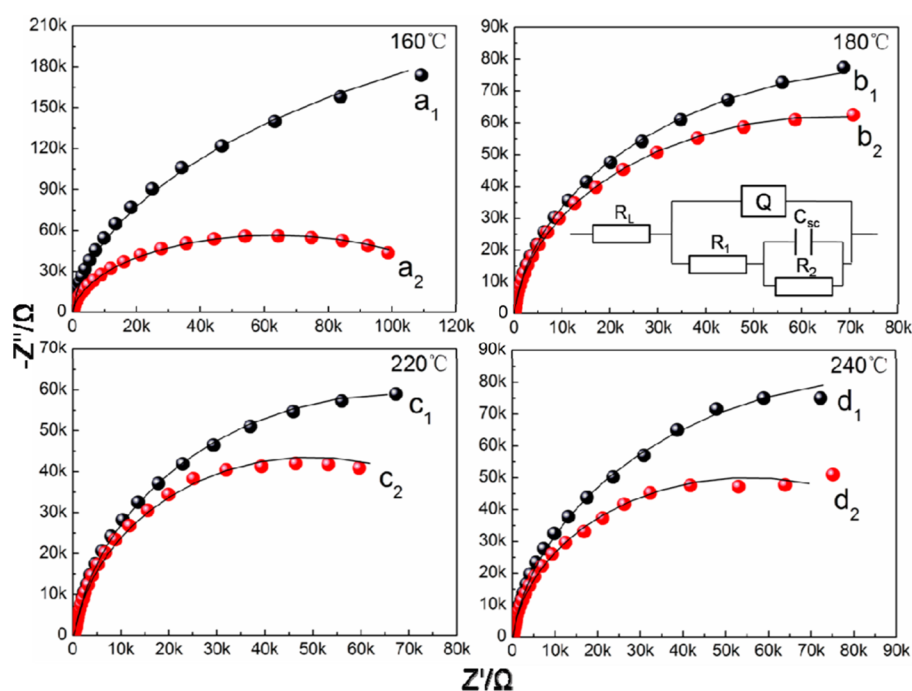
Figure 7. EIS Nyquist plots (data points) and Z-fit equivalent circuit (curve) of NF/BWO films at different temperatures.

Table 2. Z-fit Equivalent Circuit Data of NF/BWO Sample (0.25 mmol NH₄F) at Different Reaction Temperatures

CDC code	R_L (Ω)	Q (Ssec^n)	n	R_1 (Ω)	C (μF)	R_2 (kΩ)
160 °C (dark)	122.8	1.98×10^{-6}	0.6020	97.12	9.416	540.30
160 °C (UV-vis)	154.5	3.01×10^{-6}	0.6415	58.03	9.425	131.90
180 °C (dark)	131.0	2.31×10^{-5}	0.9562	163700	730.7	2810
180 °C (UV-vis)	132.4	2.28×10^{-5}	0.9581	132300	1053	2151
220 °C (dark)	178.6	2.16×10^{-5}	0.9092	14750	2.884	119.60
220 °C (UV-vis)	179.8	2.12×10^{-5}	0.9124	13370	3.343	85.43
240 °C (dark)	143.5	1.64×10^{-5}	0.9012	28.05	5.201	183.20
240 °C (UV-vis)	146.5	2.06×10^{-5}	0.9349	11900	1.182	98.52

CDC code, such as R(Q(R(RC))), could well explain the behavior of electrode process under illumination.[46,47] The EIS spectra was fitted using Z-fit equivalent circuit having the components of space charge capacitance (C_{SC}), electrochemical double-layer capacitance (Q), solution resistance (R_L), electrolytic resistance (R_1), and charge-transfer resistance (R_2). It could be seen from Figure 7 (curve) and Table 2 that fitting results were essentially coincident with the observed value (data points in Figure 7), indicating that CDC code R(Q(R(RC))) could well explain the behavior of electrode process under illumination. The value of R_2 prepared at 220 and 240 °C was reduced from 119.60 kΩ and 183.20 kΩ to 85.43 kΩ and 98.52 kΩ, respectively (see Table 2). This phenomenon fully proved the efficient charge separation and better electron transport properties at higher temperature, in accordance with the photocatalytic activities.

The migration ability of photogenerated carriers can be detected using the photocurrent, whose rate is related to the recombination rate of electron–hole pairs in the photocatalyst.[48] Studies by Endo showed that the increase of migration velocity of the electron in CB would lead to easy migration of photogenerated carriers to the surface and result in oxidation reduction reaction.[49] The amperometric current–voltage (i–t) curve was used to investigate the current densities of the four films in a potential range from 0 to 1.2 V vs Ag/

AgCl, shown in Figure 8. Under simulated sunlight irradiation, the photocurrent of the samples prepared at 160−240 °C increased gradually. Thus, the sample prepared at higher temperatures (220 and 240 °C) clearly could effectively promote the separation of photogenerated carriers, which was consistent with the results of the EIS spectra. However, the
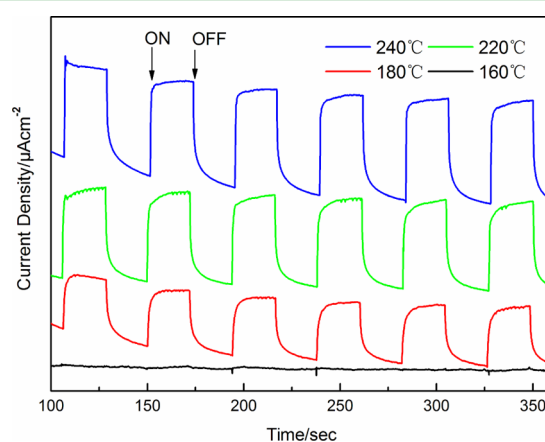

Figure 8. Amperometric current–time (i–t) curve for NF/BWO films at different temperatures.

defects of $Bi_2O_3/Bi_2WO_{6-x}F_{2x}$ prepared at 240 °C would increase, which became the trapping agent to electron—hole pairs, resulting in the greater recombination rate and the lower photocatalytic activity than that of 220 °C.

3.3. Photocatalytic Mechanism Research. Based on the results above, a possible charge separation process over $Bi_2O_3/Bi_2WO_{6-x}F_{2x}$ composites is shown in Scheme1. Bi_2O_3 is a *p*-

Scheme 1. Mechanism for the Possible Charge Separation Process over $Bi_2O_3/Bi_2WO_{6-x}F_{2x}$ Heterojunction Composites under Simulated Sunlight Irradiation
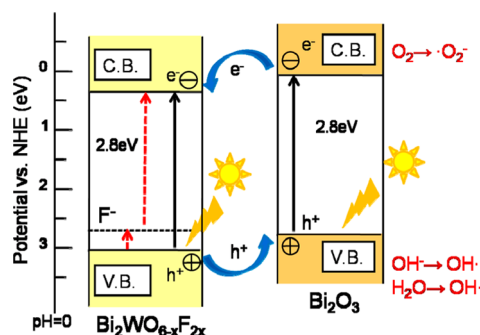
type semiconductor with a band gap of 2.8 eV.[50] As a *p—n* heterojunction, its highly reactive species, such as $\bullet O^{2-}$ and OH$\bullet$ radicals, may act as initiators of oxidation reactions.[51] When the $Bi_2O_3/Bi_2WO_{6-x}F_{2x}$ composite was irradiated under simulated sunlight, the electron in the valence band (VB) of $Bi_2WO_{6-x}F_{2x}$ was excited to its conduction band (CB). Because the VB level of Bi_2WO_6 was 0.25 eV lower than that of Bi_2O_3, the holes in the VB of $Bi_2WO_{6-x}F_{2x}$ could be transferred to that of Bi_2O_3. Simultaneously, Bi_2O_3 was used mainly as an electron-donating semiconductor. As a result, this electron—hole transfer would reduce the chance of recombination with electron formed in the CB of the excited Bi_2WO_6 under visible light. Also, NH_4F introducing the F 1s impurity level would reduce the band gap of $Bi_2WO_{6-x}F_{2x}$, which would utilize light more effectively and led to the multistep reactions. In addition, the $Bi_2O_3/Bi_2WO_{6-x}F_{2x}$ composites were assembled by nanosheets, which were beneficial for promoting the photocatalytic efficiency, because more electron holes could be separated, transferred to the surface, and reacted with RhB molecules.[52]

4. CONCLUSION

In summary, a simple one-step microwave hydrothermal method has been used to synthesize NF/BWO powders at different reaction temperatures; doping with NH_4F, and their photoelectric activities, have also been investigated. It is found that the NF/BWO powders with different crystal phases and morphologies can be prepared by varying reaction temperature of the system. The $Bi_2O_3/Bi_2WO_{6-x}F_{2x}$ hererojunction is prepared at high temperatures (220 and 240 °C) and almost-complete (>95%) photodegradation of RhB under the exposure of simulated sunlight is achieved within 90 min with the $Bi_2O_3/Bi_2WO_{6-x}F_{2x}$ heterojunction prepared at 220 °C. The as-prepared $Bi_2O_3/Bi_2WO_{6-x}F_{2x}$ heterojunction exhibits obviously enhanced photocatalytic activity, because of its generated impurity level and the existence of the *p—n* junction between *p*-type Bi_2O_3 and *n*-type Bi_2WO_6. The electrochemical impedance spectroscopy (EIS) and photocurrent results also prove that efficient charge separation and better electron transport properties are achieved by the $Bi_2O_3/Bi_2WO_{6-x}F_{2x}$ hetero-

junction film prepared at 220 °C. The study provides a simple and popular method in the fabrication of the composite with the ion-doped heterostructure, which may show a variety of applications.

■ AUTHOR INFORMATION

Corresponding Author
*E-mail: tan3114@163.com.

Notes
The authors declare no competing financial interest.

■ REFERENCES

(1) Zhang, X. M.; Chang, X. F.; Gondal, M. A.; Zhang, B.; Liu, Y. S. Synthesis and Photocatalytic Activity of Graphene/BiOBr Composites under Visible Light. *Appl. Surf. Sci.* **2012**, *258*, 7826−7832.

(2) Fang, J.; Wang, F.; Qian, K.; Bao, H. Z.; Jiang, Z. Q.; Huang, W. X. Bifunctional N-Doped Mesoporous TiO$_2$ Photocatalysts. *J. Phys. Chem. C* **2008**, *112*, 18150−18156.

(3) Song, X. C.; Zheng, Y. F.; Ma, R.; Zhang, Y. Y.; Yin, H. Y. Photocatalytic Activities of Mo-Doped Bi$_2$WO$_6$ Three-Dimensional Hierarchical Microspheres. *J. Hazard. Mater.* **2011**, *192*, 186−191.

(4) Jiang, L.; Wang, L. Z.; Zhang, J. L. A Direct Route for the Synthesis of Nanometer-Sized Bi$_2$WO$_6$ Particles Loaded on a Spherical MCM-48 Mesoporous Molecular Sieve. *Chem. Commun.* **2010**, *46*, 8067−8069.

(5) Zhang, Z. J.; Wang, W. Z.; Yin, W. Z.; Shang, M.; Wang, L.; Sun, S. M. Inducing Photocatalysis by Visible Light Beyond the Absorption Edge: Effect of Upconversion Agent on the Photocatalytic Activity of Bi$_2$WO$_6$. *Appl. Catal., B* **2010**, *101*, 68−73.

(6) Wang, C. Y.; Zhang, H.; Li, F.; Zhu, L. Y. Degradation and Mineralization of Bisphenol A by Mesoporous Bi$_2$WO$_6$ under Simulated Solar Light Irradiation. *Environ. Sci. Technol.* **2010**, *44*, 6843.

(7) Zhang, Z. J.; Wang, W. Z.; Shang, M.; Yin, W. Z. Low-Temperature Combustion Synthesis of Bi$_2$WO$_6$ Nanoparticles as a Visible-Light-Driven Photocatalyst. *J. Hazard. Mater.* **2010**, *177*, 1013−1018.

(8) Fu, H. B.; Zhang, L. W.; Yao, W. Q.; Zhu, Y. F. Photocatalytic Properties of Nanosized Bi$_2$WO$_6$ Catalysts Synthesized Via a Hydrothermal Process. *Appl. Catal., B* **2006**, *66*, 100−110.

(9) Takeda, H.; Nishida, T.; Okamura, S.; Shiosaki, T. Crystal Growth of Bismuth Tungstate Bi$_2$WO$_6$ by Slow Cooling Method Using Borate Fluxes. *J. Eur. Ceram. Soc.* **2005**, *25*, 2731−2734.

(10) Ren, J.; Wang, W. Z.; Sun, S. M.; Zhang, L.; Chang, J. Enhanced Photocatalytic Activity of Bi$_2$WO$_6$ Loaded with Ag Nanoparticles under Visible Light Irradiation. *Appl. Catal., B* **2009**, *92*, 50−55.

(11) Zhu, S. B.; Xu, T. G.; Fu, H. B.; Zhao, J. C.; Zhu, Y. F. Synergetic Effect of Bi$_2$WO$_6$ Photocatalyst with C-60 and Enhanced Photoactivity under Visible Irradiation. *Environ. Sci. Technol.* **2007**, *41*, 6234−6239.

(12) Xiao, Q.; Zhang, J.; Xiao, C.; Tan, X. K. Photocatalytic Degradation of Methylene Blue over Co$_3$O$_4$/Bi$_2$WO$_6$ Composite under Visible Light Irradiation. *Catal. Commun.* **2008**, *9*, 1247−1253.

(13) Shang, M.; Wang, W. Z.; Zhang, L.; Sun, S. M.; Wang, L.; Zhou, L. 3D Bi$_2$WO$_6$/TiO$_2$ Hierarchical Heterostructure: Controllable Synthesis and Enhanced Visible Photocatalytic Degradation Performances. *J. Phys. Chem. C* **2009**, *113*, 14727−14731.

(14) Zhang, L. S.; Wong, K. H.; Chen, Z. G.; Yu, J. C.; Zhao, J. C.; Hu, C.; Chan, C. Y.; Wong, P. K. AgBr–Ag–Bi$_2$WO$_6$ Nanojunction System: A Novel and Efficient Photocatalyst with Double Visible-Light Active Components. *Appl. Catal., A* **2009**, *363*, 221−229.

(15) Long, M. C.; Cai, W. M.; Cai, J.; Zhou, B. X.; Chai, X. Y.; Wu, Y. H. Efficient Photocatalytic Degradation of Phenol over Co$_3$O$_4$/BiVO$_4$ Composite under Visible Light Irradiation. *J. Phys. Chem. B* **2006**, *110*, 20211−20216.

(16) Chai, S. Y.; Kim, Y. J.; Jung, M. H.; Chakraborty, A. K.; Jung, D.; Lee, W. I. Heterojunctioned BiOCl/Bi$_2$O$_3$, A New Visible Light Photocatalyst. *J. Catal.* **2009**, *262*, 144.

(17) Bessekhouad, Y.; Robert, D.; Weber, J.-V. Bi$_2$S$_3$/TiO$_2$ and CdS/TiO$_2$ Heterojunctions as an Available Configuration for Photocatalytic Degradation of Organic Pollutant. *J. Photochem. Photobiol., A* **2004**, *163*, 569−580.

(18) Obregon, S.; Colon, G. Erbium Doped TiO$_2$−Bi$_2$WO$_6$ Heterostructure with Improved Photocatalytic Activity under Sun-Like Irradiation. *Appl. Catal., B* **2013**, *140*, 299−305.

(19) Murcia López, S.; Hidalgo, M. C.; Navío, J. A.; Colón, G. Novel Bi$_2$WO$_6$−TiO$_2$ Heterostructures for Rhodamine B Degradation under Sunlike Irradiation. *J. Hazard Mater.* **2011**, *185*, 1425−1434.

(20) Fu, G. K.; Xu, G. N.; Chen, S. P.; Lei, L.; Zhang, M. L. Ag$_3$PO$_4$/Bi$_2$WO$_6$ Hierarchical Heterostructures with Enhanced Visible Light Photocatalytic Activity for the Degradation of Phenol. *Catal. Commun.* **2013**, *40*, 120−124.

(21) Yang, W. J.; Ma, B.; Wang, W. C.; Wen, Y. W.; Zeng, D. W.; Shan, B. Enhanced Photosensitized Activity of a BiOCl−Bi$_2$WO$_6$ Heterojunction by Effective Interfacial Charge Transfer. *Phys. Chem. Chem. Phys.* **2013**, *15*, 19387−19394.

(22) Yu, C. L.; Yang, K.; Yu, J. C.; Cao, F. F.; Li, X.; Zhou, X. C. Hydrothermal Synthesis and Photocatalytic Performance of Bi$_2$WO$_6$/ZnO Heterojunction Photocatalysts. *J. Inorg. Mater.* **2011**, *26*, 1157−1163.

(23) Ge, M.; Li, Y. F.; Liu, L.; Zhou, Z.; Chen, W. Bi$_2$O$_3$−Bi$_2$WO$_6$ Composite Microspheres: Hydrothermal Synthesis and Photocatalytic Performances. *J. Phys. Chem. C* **2011**, *115*, 5220−5225.

(24) Gui, M. S.; Zhang, W. D.; Su, Q. X.; Chen, C. H. Preparation and Visible Light Photocatalytic Activity of Bi$_2$O$_3$/Bi$_2$WO$_6$ Heterojunction Photocatalysts. *J. Solid State Chem.* **2011**, *184*, 1977−1982.

(25) Li, X. N.; Huang, R. K.; Hu, Y. H.; Chen, Y. J.; Liu, W. J.; Yuan, R. S. A Templated Method to Bi$_2$WO$_6$ Hollow Microspheres and Their Conversion to Double-Shell Bi$_2$O$_3$/Bi$_2$WO$_6$ Hollow Microspheres with Improved Photocatalytic Performance. *Inorg. Chem.* **2012**, *51*, 6245−6250.

(26) Zhang, D. F.; Zhang, H.; Shang, Y.; Guo, L. Stoichiometry-Controlled Fabrication of Cu$_x$S Hollow Structures with Cu$_2$O as Sacrificial Templates. *Cryst. Growth. Des.* **2011**, *11*, 3748−3753.

(27) Tan, G. Q.; Zhang, L. L.; Ren, H. J.; Wei, S. S.; Huang, J.; Xia, A. Effects of pH on the Hierarchical Structures and Photocatalytic Performance of BiVO$_4$ Powders Prepared via the Microwave Hydrothermal Method. *ACS Appl. Mater. Interfaces* **2013**, *5*, 5186−5193.

(28) Lai, K. R.; Wei, W.; Zhu, Y. T.; Guo, M.; Dai, Y.; Huang, B. B. Effects of Oxygen Vacancy and N-doping on the Electronic and Photocatalytic Properties of Bi$_2$MO$_6$ (M = Mo, W). *J. Solid State Chem.* **2012**, *187*, 103−108.

(29) Chauhan, S.; Kumar, M.; Chhoker, S.; Katyal, S. C.; Singh, H.; Jewariya, M.; Yadav, K. L. Multiferroic, Magnetoelectric and Optical Properties of Mn Doped BiFeO$_3$ Nanoparticles. *Solid State Commun.* **2012**, *152*, 525−529.

(30) Chakrabarti, K.; Das, K.; Sarkar, B.; Ghosh, S.; De, S. K.; Sinha, G.; Lahtinen, J. Enhanced Magnetic and Dielectric Properties of Eu and Co Co-Doped BiFeO$_3$ Nanoparticles. *Appl. Phys. Lett.* **2012**, *101*, 042401.

(31) Knight, K. S. The Crystal Structure of Russellite, a Re-Determination Using Neutron Powder Diffraction of Synthetic Bi$_2$WO$_6$. *Mineral. Mag.* **1992**, *56*, 399.

(32) Battle, P. D.; Catlow, C. R. A.; Drennans, J.; Murray, A. D. The Structural Properties of the Oxygen Conducting δ phase of Bi$_2$O$_3$. *J. Phys. C: Solid State Phys.* **1983**, *16*, L561.

(33) Champarnaud-Mesjard, J. C.; Frit, B.; Watanabe, A. Crystal Structure of Bi$_2$W$_2$O$_9$, The n = 2 Member of the Homologous Series (Bi$_2$O$_2$)B$^{VI}_n$O$_{3n+1}$ of Cation-Deficient Aurivillius Phases. *J. Mater. Chem.* **1999**, *9*, 1319−1322.

(34) Maczka, M.; Macalik, L.; Hermanowicz, K.; Kepiński, L.; Tomaszewski, P. Phonon Properties of Nanosized Bismuth Layered Ferroelectric Material—Bi$_2$WO$_6$. *J. Raman Spectrosc.* **2010**, *41*, 1059−1066.

(35) Huang, H.; Chen, H.; Xia, Y.; Tao, X.; Gan, Y.; Weng, X.; Zhang, W. Controllable Synthesis and Visible-Light-Responsive Photocatalytic Activity of Bi$_2$WO$_6$ Fluffy Microsphere with Hierarchical Architecture. *J. Colloid Interface Sci.* **2012**, *370*, 132−138.

(36) Zhang, L. W.; Wang, Y. J.; Cheng, H. Y.; Yao, W. Q.; Zhu, Y. F. Synthesis of Porous Bi$_2$WO$_6$ Thin Films as Efficient Visible-Light-Active Photocatalysts. *Adv. Mater.* **2009**, *21*, 1286−1290.

(37) Crane, M. R.; Frost, L.; Williams, P. A.; Kloprogge, J. T. Raman Spectroscopy of the Molybdate Minerals Chillagite (Tungsteinian Wulfenite-I4), Stolzite, Scheelite, Wolframite and Wulfenite. *J. Raman Spectrosc.* **2002**, *33*, 62.

(38) Rubbens, A.; Drache, M.; Roussel, P.; Wignacourt, J. P. Wignacourt Raman Scattering Characterization of Bismuth Based Mixed Oxides with Bi$_2$O$_3$ Related Structures Mater. *Mater. Res. Bull.* **2007**, *42*, 1683−1690.

(39) Huang, J.; Tan, G. Q.; Xia, A.; Ren, H. J.; Zhang, L. L. Growth Mechanism and Photocatalytic Properties of Flower-Like Bi$_2$WO$_6$ Powders Synthesized by a Microwave Hydrothermal Method. *Res. Chem. Intermed.* **2014**, *40*, 903−911.

(40) Wu, J.; Duan, F.; Zheng, Y.; Xie, Y. Synthesis of Bi$_2$WO$_6$ Nanoplate-Built Hierarchical Nest-like Structures with Visible-Light-Induced Photocatalytic Activity. *J. Phys. Chem. C* **2007**, *111*, 12866−12871.

(41) Moulder, J. F.; Stickle, W. F.; Sobol, P. E.; Bomben, K. D. *Handbook of X-ray Photoelectroscopy*; Physical Electronics, Inc.: Chanhassen, MN, 1995.

(42) Li, X. N.; Huang, R. K.; Hu, Y. H.; Chen, Y. J.; Liu, W. J.; Yuan, R. S.; Li, Z. H. A Templated Method to Bi$_2$WO$_6$ Hollow Microspheres and Their Conversion to Double-Shell Bi$_2$O$_3$/Bi$_2$WO$_6$ Hollow Microspheres with Improved Photocatalytic Performance. *Inorg. Chem.* **2012**, *51*, 6245−6250.

(43) Zhang, W. D.; Jiang, L. C.; Ye, J. S. Photoelectrochemical Study on Charge Transfer Properties of ZnO Nanowires Promoted by Carbon Nanotubes. *J. Phys. Chem. C* **2009**, *113*, 16247−16253.

(44) Liu, H.; Cheng, S.; Wu, M.; Wu, H.; Zhang, J.; Li, W.; Cao, Ch. Photoelectrocatalytic Degradation of Sulfosalicylic Acid and Its Electrochemical Impedance Spectroscopy Investigation. *J. Phys.Chem. A* **2000**, *104*, 7016−7020.

(45) Yang, J.; Li, W.; Li, J.; Sun, D.; Chen, Q. Hydrothermal Synthesis and Photoelectrochemical Properties of Vertically Aligned Tungsten Trioxide (Hydrate) Plate-Like Arrays Fabricated Directly on FTO Substrates. *J. Mater. Chem.* **2012**, *22*, 17744−17752.

(46) Yun, H. J.; Lee, H.; Joo, J. B.; Kim, W.; Yi, J. The Effect of The Preparation Condition of TiO$_2$ Colloids on Their Surface Structures. *J. Phys. Chem. C* **2009**, *113*, 3050−3055.

(47) Gomes, W. P.; Vanmaekelbergh, D. Impedance Spectroscopy at Semiconductor Electrodes: Review and Recent Developments. *Electrochim. Acta* **1996**, *41*, 967.

(48) Kim, H. G.; Borse, P. H.; Choi, W.; Lee, J. S. Photocatalytic Nanodiodes for Visible-Light Photocatalysis. *Angew. Chem., Int. Ed.* **2005**, *44*, 4585−4589.

(49) Endo, T.; Kobayashi, T.; Sato, T.; Shimada, M. High Pressure Synthesis and Electrical Properties of BaTiO$_{3-x}$F$_x$. *J. Mater. Sci.* **1990**, *25*, 619−623.

(50) Bian, Z. F.; Zhu, J.; Wang, S. H.; Cao, Y.; Qian, X. F.; Li, H. X. Self-Assembly of Active Bi$_2$O$_3$/TiO$_2$ Visible Photocatalyst with Ordered Mesoporous Structure and Highly Crystallized Anatase. *J. Phys. Chem. C* **2008**, *112*, 6258−6262.

21049

dx.doi.org/10.1021/am505817h | *ACS Appl. Mater. Interfaces* 2014, 6, 21041−21050

(51) Hameed, A.; Montini, T.; Gombac, V.; Fornasiero, P. Surface Phases and Photocatalytic Activity Correlation of Bi_2O_3/Bi_2O_{4-x} Nanocomposite. *J. Am. Chem. Soc.* **2008**, *130*, 9658.

(52) Hagfeldt, A.; Gratzel, M. Light-Induced Redox Reactions in Nanocrystalline Systems. *Chem. Rev.* **1995**, *95*, 49−68.

21050

dx.doi.org/10.1021/am505817h | *ACS Appl. Mater. Interfaces* 2014, 6, 21041−21050